Remote sensing and modeling analysis of the extreme dust storm hitting Middle East and Eastern Mediterranean in September 2015

Solomos Stavros[1], Albert Ansmann[2], Rodanthi-Elisavet Mamouri[3], Ioannis Binietoglou[1,5], Platon Patlakas[4], Eleni Marinou[1,6] and Vassilis Amiridis[1]

[1]Institute for Astronomy, Astrophysics, Space Applications and Remote Sensing (IAASARS), National Observatory of Athens, Athens, Greece
[2]Leibniz Institute for Tropospheric Research, Leipzig, Germany
[3]Cyprus University of Technology, Department of Civil Engineering and Geomatics, Limassol, Cyprus
[4]School of Physics, Division of Environment and Meteorology, University of Athens, Athens, Greece
[5]National Institute of R&D for Optoelectronics, Magurele, Ilfov, Romania
[6]Laboratory of Atmospheric Physics, Physics Department, Aristotle University of Thessaloniki, 54124, Thessaloniki, Greece

Abstract The extreme dust storm that affected Middle East and the Eastern Mediterranean in September 2015 resulted in record-breaking dust loads over Cyprus with aerosol optical depth exceeding 5.0 at 550 nm. We analyze this event using profiles from the European Aerosol Research Lidar Network (EARLINET), the Cloud-Aerosol Lidar and Infrared Pathfinder Satellite Observation (CALIPSO), geostationary observations from the Meteosat Second Generation - Spinning Enhanced Visible and Infrared Imager (MSG-SEVIRI) and high resolution simulations with the Regional Atmospheric Modeling System (RAMS). The analysis reveals the main mechanisms that resulted in the generation and persistence of the dust cloud over Middle-East and Cyprus. A combination of meteorological and surface processes is found: (a) the development of a thermal low at the area of Syria that results in unstable atmospheric conditions and dust mobilization at this area, (b) the convective activity over North Iraq that triggers the formation of a westward moving haboob that merges with the previously elevated dust layer; and (c) the changes in land use due to war at the areas of North Iraq and Syria that enhances dust erodibility.

1. Introduction

A record dust storm affected the entire Middle East and Cyprus in September 2015. Remote sensing observations and in-situ measurements of Arabian dust from this episode during 7-11 September 2015 are presented by Mamouri et al. (2016) for the station of Limassol (34.7°N, 33°E). As reported in their article, the extreme amounts of dust over Middle East and East Mediterranean originate from the desert and arid areas of Syria and North Iraq. Triggered by this work, we analyze here the main processes that resulted in the mobilization of dust due to a combination of cyclonic flow and haboob formation.

Haboobs are local and mesoscale atmospheric density currents that mobilize huge amounts of dust and create a propagating dust wall extending up to 2-3 km in the troposphere (Knippertz et al., 2009; Solomos et al., 2012). These systems are well known by local populations at desert and arid areas worldwide due to their devastating impact in visibility and human health (e.g. Schepanski et al., 2009; Emmel et al., 2010). The responsible mechanism for haboob formation is the generation of a cold pool of ambient air due to evaporative cooling. The rain and ice condensates evaporate (or melt) as they fall through the warmer and unsaturated air and the absorption of latent heat from the phase changes leads in a vigor cooling of the surrounding air. When these convective outflow boundaries travel over bare soil and desert areas they result in the generation of a propagating dust wall. The scale of the processes that participate in the generation of such atmospheric density currents ranges from synoptic down to mesoscale and local. As a result, haboobs and their effects in weather and air-quality cannot be resolved by the coarse global model resolutions (Marsham et al., 2013). Moreover, haboobs usually generate over remote arid areas where no in-situ networks are present and inside dust-storm measurements can only be obtained during field campaign experiments (e.g. SAMUM 1 & 2, Ansmann et al., 2011; FENNEC, Ryder et al., 2015). Following these limitations, most of the efforts for the studying and forecasting of such intense dust episodes rely on passive and active remote sensing observations (e.g. MODIS, EARLINET, CALIPSO) and on high resolution modeling simulations. It is also worth to mention that satellite data assimilation, which has been shown to improve dust forecasts in global models (Benedetti, et al., 2009), cannot be easily adopted for the description of haboobs. The reason is that even when the correct amounts of dust are assimilated in the dust model, the model itself will not be able to determine the dust transport since the primary atmospheric properties of moisture convergence and wind gust remain unresolved.

A variety of studies on haboobs has been performed worldwide. Knippertz et al. (2009); Reinfried et al. (2009); Solomos et al. (2012); Roberts and Knippertz (2014), analyzed the physical processes that lead in severe haboob formation in Sahara as an aftermath of Atlas Mountains convective storms. Bou Karam et al. (2008) showed the contribution of the east Atlantic monsoon flow and the associated mesoscale convective systems (MCS) in dust elevation along the Sahel. Vukovic et al. (2014) described the severe convective dust storm that hit Phoenix Arizona in July 2011. Asian haboobs from the Taklimakan and Gobi deserts are described and simulated in Takemi, (1999, 2005). All these studies agree in the complexity and synergy between various physical processes at multiple atmospheric scales that govern the generation and lifetime of these systems. Apart from their devastating effects at local and near surface scales, such events may also contribute to the free-troposphere dust burden in several ways: First, entrainment of dust particles in the free troposphere takes place at the turbulent region of the density current head (Takemi, 2005; Solomos et al., 2012); Second, they trigger secondary convective cells along their pathways that may evolve to synoptic scale dust events and third, dust residuals remain aloft after the cold pool declines.

The current article is the second part (Part 2) in a series of articles on the September 2015 extraordinary dust storm in Middle East and Eastern Mediterranean. In Part 1, Mamouri et al. (2016) present a detailed analysis of remote sensing and in-situ monitoring of the event over Cyprus. The formation of similar events is not fully understood and we use this unique episode to elucidate the mechanism of dust production in this understudied region. EARLINET measurements along with CALIPSO and MSG observations are used to fine tune RAMS simulations and explain the physical processes that resulted in this haboob-driven dust storm. We focus our analysis on the first two days of the event (6 and 7 September 2015) when the extraordinary dust-storm was generated. To the best of our knowledge this is the first detailed modeling and remote sensing study to describe a Middle East haboob. The modeling and measurement techniques for the analysis are presented in Section 2. Section 3 includes the model results, the remote sensing observations and the investigation of the atmospheric processes that lead in the formation of the dust episode. Conclusive remarks and discussion are presented in Section 4.

2. Instruments and models.

2.1 Remote sensing observations

2.1.1. EARLINET

The lidar station at Limassol (34.7° N, 33° E; 23 m above sea level, a.s.l.) is part of the European Aerosol Research Lidar Network (EARLINET: Pappalardo et al., 2014). Details on the lidar station equipment and the retrieval algorithms are given in Mamouri et al. (2016). Dust mass concentration profiles are obtained from the dust optical properties following the methodology proposed by Ansmann et al. (2012). For this case study we use a lidar ratio of 40 sr that is typical for Middle East dust (Mamouri et al., 2013). The overall uncertainty in the estimated dust mass concentrations is 20-30%. → provide here more details and reference papers.

2.1.2. CALIPSO

CALIOP, the principal instrument on board the CALIPSO satellite is a standard dual-wavelength (532 and 1064 nm) backscatter lidar, operating a polarization channel at 532 nm (Winker et al., 2009). CALIOP has been acquiring high-resolution profiles of the attenuated backscatter at 532 and 1064 nm along with polarized backscatter in the visible channel since 2006. After calibration and range correction of the lidar backscatter signals (Level 1 CALIPSO product), cloud and aerosol layers are identified and aerosol backscatter and extinction coefficient profiles at 532 and 1064 nm are retrieved as part of the Level 2 CALIPSO product. The CALIPSO algorithms are described in detail ~~in a special issue of the Journal of Atmospheric and Oceanic Technology (e.g.~~ Winker et al., 2009). In this study, we utilize L2 version 3 Aerosol and Cloud profiles product at a horizontal resolution of 5 km analysis and vertical resolution of 60 m (in altitudes up to 8 km above sea level). In extreme haboob events, where the optical signal is very high, it is possible for the algorithm to wrongly attribute a dust layer as a cloud. In order to address this issue and fully understand the observed scene we use collocated information derived from MSG-SEVIRI (see sect. 2.1.3). In the two CALIPSO cases used here, MSG-SEVIRI RGB images confirmed that CALIPSO overpasses was cloud free, hence we classify both aerosol and cloud categorized CALIPSO observations as aerosol. Moreover, both of the cases have significantly high particle depolarization ratio values, which is a signature of pure dust scenes. In order convert the dust extinction coefficient from CALIPSO into dust mass concentration, we follow the methodology proposed by Ansmann et al. (2012) using the conversion parameter of desert dust that is proposed in Mamouri and Ansmann (2017).

2.1.3. MSG-SEVIRI

The Meteosat dust RGB composite is produced from a combination between three MSG channels: IR12.0-IR10.8 (red), IR10.8-IR8.7 (green) and IR10.8 (blue). This product is provided in hourly intervals by EUMETSAT (European Organisation for the Exploitation of Meteorological Satellites) and aims in the monitoring of dust transport. Dust in these RGB images appears in pink or magenta colors while green-blue and red-brown colors are reserved for land and clouds respectively (Lensky and Rosenfeld, 2008).

2.2 Modeling simulations

2.2.1 RAMS-ICLAMS model

For the simulations used in this study we adopt the online coupled atmospheric and air quality modeling system RAMS-ICLAMS (Pielke et al., 1992; Meyers et al., 1997; Cotton et al., 2003; Solomos et al., 2011). The Integrated Community Limited Area Modeling System (ICLAMS) is an enhanced version of RAMS6.0 and it has been developed by the Atmospheric Modeling and Weather Forecasting Group at the University of Athens, Greece. The model is set up in a two-way nesting configuration. The external domain grid space is set at 12×12 km and the grid space of the inner domain is set at 4×4 km. A higher resolution (cloud resolving) grid at 2×2 km is nested over the haboob generation area at Syria-Iraq-Iran-Turkey borders. The locations of the model domains are shown in Figure 1b. The vertical structure of the model consists of 50 terrain following levels stretching from the surface up to 18 km. The dust production scheme follows the saltation and bombardment approach (Marticorena and Bergametti 1995; Spyrou et al., 2010). Wet and dry deposition of dust is formulated following Seinfeld and Pandis 1998. Mineral dust is represented with a transport mode of eight radii bins namely 0.15, 0.25, 0.45, 0.78, 1.3, 2.2, 3.8 and 7.1 μm. Sea salt aerosol is also parameterized following Monahan et al., 1986; Zhang et al., 2005; Leeuw et al., 2000 and Gong et al., 2002, 2003 and it is represented with an accumulated and a coarse mode at 0.18 μm and 1.425 μm in radius respectively. Dust and sea salt particles interact with the radiative transfer code of the model (Rapid Radiative Transfer Model (RRTM), Mlawer et al., 1997; Iacono et al., 2000) for the computation of heating rate fluxes. The formation of cloud condensation nuclei (CCN) and ice nuclei (IN) from dust and sea salt particles is also included in the model based on the schemes of Fountoukis and Nenes, 2005 and Barahona and Nenes 2009. Initial and boundary conditions are from the NCEP final analysis dataset (FNL at 1°×1° resolution) and the sea surface temperature is the NCEP operational SST at 0.5°×0.5°. The convective parameterization scheme of Kain and Fritsch, 1993 (KF) is activated for the two coarser grids. Assimilation of radiosonde data from the airports of Adana (36.98°N, 35.35°E), Bet Dagan (32.00°N, 34.81°E), Diyarbakir (37.54°N, 40.12°E), Mafraq (32.36°N, 36.25°E) and Nicosia (35.10°N, 33.30°E) is also activated to fine tune the simulations. A series of sensitivity runs with various model configurations (different physical schemes, assimilation parameters and domain structures) is performed until we conclude to the optimum setup for the specific simulation.

2.2.2 Land use changes and activation of dust sources

An accurate representation of dust sources in the region is crucial for understanding this complex dust event, but this is hampered by recent land cover changes in the region. The original land use database of the model is the USGS Data Base Version 2 which is obtained from 1-km AVHRR data (Advanced Very High Resolution Radiometer) spanning April 1992 through March 1993. However, complex interactions of drier climate (Notaro et al., 2015; Cook et al., 2016), transboundary water managements (Voss et al., 2013), and prolonged conflict (Jaafar and Woertz, 2016) have led to change of land use types that are no longer reflected at the model and this could have a large impact on dust production. The comparison of Landsat 8 natural color and NDVI imagery between 2013 and 2015 (Figure 2) reveals large areas of uncultivated fields in regions of contested boarders and exposed river and lake-bed sediments especially around the Euphrates river, all of which are known to be very efficient dust sources (Prospero et al, 2002; Ginoux et al., 2012). In order to get most accurate representation of dust sources for the specific event we use 1km monthly Normalized Difference Vegetation Index (NDVI) from MODIS (Didan K., 2015) to characterize land use type in the region of interest. Specifically, we consider regions with NDVI values from 0 to 0.1 to correspond to bare soil and consequently efficient dust sources (DeFries et al., 1994). The updated land cover dataset is used for all results shown in this study. Results from simulations using the older database are only shown in Figure 11 for comparison.

3. Results

3.1 Meteorological conditions

The main driving force for the generation of this extreme dust episode is the combination between two distinct meteorological features in the greater area: (i) establishment of a thermal low over the bare-soil areas of Syria and (ii) convective outflow boundaries at the mountains of Iraq and Syria. These processes are analyzed in the following sections using modeling results and remote sensing observations.

3.1.1 Development of a low pressure system over Syria on 6 September 2015

As seen at the outer model grid in Figure 1a, the passage of a trough is evident over Turkey on 6 September 2015, 00:00 UTC. The low pressure center at 500mb is found at 5840 m over the east bank of Black Sea. During the same day, radiative warming of the bare soil surface results in very hot soil temperatures exceeding 50 °C in Syria and Iraq. This combination of cold air aloft with low level warming, leads in the formation of a thermal low pressure system over Syria. Another parameter that plays important role for the process of dust source activation is the difference between surface temperature (T_{Surf}) and air temperature at 2m (T_{2m}). Findings from earlier field experiments (i.e. SAMUM) show that such a difference of 17°C-20°C facilitates the uplift of convective dust plumes (Ansmann et al., 2009). As seen in Figure 1b, the modeled T_{Surf}-T_{2m} difference at 10:00 UTC exceeds 17°C over extended bare soil areas in Syria. This temperature gradient further explains the effectiveness of dust production at these areas. The pressure system and the associated cyclonic flow persist during the entire day of 6th September 2015 and result in the mobilization of dust in the area. The low pressure system is evident by the 850 mb geopotential height contours in Figure 3a, reaching a minimum of 1490 m at 08:00 UTC, 6 September 2015. Dust uptake is mostly evident at the outer parts of the cyclone where surface wind speed exceeds 7 m s^{-1} almost during the entire day and T_{Surf}-T_{2m} obtains maximum values. The elevated particles are quickly distributed inside the system and a distinct cylindrical dust cloud is soon formed. Recirculation of the elevated dust particles inside the closed cyclonic flow results in extreme AOT values exceeding 15 at specific areas as seen in Figure 3a. The formation of this dense dust plume is also evident in the MSG-SEVIRI satellite dust RGB image in Figure 3b. Pink and purple colors in this image indicate dust while brown and red colors indicate clouds. As seen in Figure 4, convergence of low level flow along the Mediterranean coastline during the morning hours on September 6th, results in local convective activity at the area of Lebanon Mountains and in local disturbance of the mesoscale wind field. A SE flow is established, and this flow is responsible for the transport of dust from Lebanon towards Cyprus that is evident at the satellite and modeling images on 7 September 2015, 00:00 UTC (Figure 5). This cut-off plume (plume_1) travels in the lower troposphere above the marine boundary layer and it was observed at 1.5 km above Limassol at 19:00 UTC on September [illegible] as reported by Mamouri et al. 2016. The faster propagating haboob plume (plume_2) also was detected at 2.0-3.5 km over Cyprus at 19:00 UTC. The extreme AOT values (>10) that are seen in Figure 5a over Syria result from the overlapping of cyclone-driven and haboob-driven dust over this area. In the model, approaching of the haboob front in Syria is accompanied also by cloud formation as seen by the 70% cloud-cover contours in Figure 5a; however these clouds are not evident in the satellite image (Figure 5b). The more elevated (cyclone-driven) dust in Figure 5b is shown in pink (plume_1 over the sea and plume_3 over North Syria and South Turkey have the same origin) and the near surface dust (haboob) is shown with a darker purple color (plume_2).

3.1.2. Convection and haboob generation on 6 and 7 September 2015

At 13:00 UTC on 6th of September a northward low level flow is evident over N. Iraq and N. Syria (Figure 6a). This relatively unstable air mass is characterized by increased equivalent potential temperature (theta_e) reaching up to 508 K. This flow is associated with a westerly shift of the Somalian Low Level Jet (SLLJ). The SLLJ is part of the West India Monsoon circulation and as shown in Figure 6b it is characterized by strong SW winds blowing from the Somalia highlands towards West India. This low level flow steers towards the west along the coastal mountains of Yemen and Oman and results in SE winds transferring moisture from the Arabian Sea towards the inlands of the Arabian Peninsula. Mechanical elevation of this relatively unstable air as it approaches Mt. Sinjar in N. Iraq (Figure 6a) triggers convection at this area. A crucial parameter that determines the formation of a cold pool is the temperature difference between rain droplets and the ambient air. As seen in Figure 7a, the absolute difference between rain droplets temperature and ambient air temperature in the model reaches a maximum of 22 °C at this area. This temperature gradient results in a faster evaporation rate of the rain droplets as they fall through the unsaturated air and in the formation of a cold pool at the area of North Iraq. Wind speed inside the cold pool ranges from 10 up to 20 ms^{-1} (Figure 7b). This cold pool moves towards the North and triggers the generation of secondary convective cells at the mountainous areas along Iran-Iraq-Turkey borderline. At 20:00 UTC, a series of convective outflows converges in an organized SE propagating density current that is evident in the model over N. Iraq and N. Syria (Figure 8a). This system is characterized by wind speeds higher than 6 m s^{-1} and results in activation of dust sources and near surface concentrations largely exceeding 10000 μg m^{-3} (Figure 8b). However, the corresponding SEVIRI image (Figure 8c) indicates that by this time the haboob has already penetrated about 200 km inside Syria which is not reproduced by the model. This latency between satellite and modeled haboob fronts is an indication that the convective downdrafts were in fact even stronger.

3.2 Dust cloud properties and comparison with observations

3.2.1. Vertical dust structure

The dust layer structure as it propagates towards the Mediterranean is captured by two CALIPSO overpasses at 23:33 UTC, 6 September 2015 (Figure 9) and at 10:35 UTC, 7 September 2015 (Figure 10). Collocated model cross sections of dust and MSG-SEVIRI dust images are also presented in Figures 8 and 9. All heights in satellite and model profiles refer to heights above surface. At the first overpass (Figure 9), the south part of the dust layer (31°N-34°N) is detected up to 2-3 km and originates from the cyclonic flow over Syria. Dust concentrations are estimated from CALIPSO backscatter and as seen in Figure 9b they reach up to 5000 μg m^{-3} close to the surface between 31°N-34°N and higher than 6000 μg m^{-3} in the first 500 m. Similar structure and dust concentrations are also found by the model (Figure 9c). The northern part of the overpass (35°N-38°N) detects also elevated dust due to cyclonic activity between 2.5-4.5 km and concentrations up to 1000-2000 μg m^{-3} are evident at this area from CALIPSO. The model overpredicts dust at this area with simulated concentrations reaching up to 5000 μg m^{-3}. These elevated layers are shown with pink colors in Figure 9a. Low level dust (purple colors in SEVIRI images) is also evident in this area due to the propagating haboob and CALIPSO detects this two-layer structure with a clear separation at 2 km. The model also reproduces the uplift of dust at 35°N where the two systems (cyclone and haboob) merge. The modeled concentration inside the haboob reaches extraordinary values exceeding 10000 μg m^{-3}. Due to the severity of the event, the CALIPSO lidar signal is totally attenuated bellow ~1 km (dark blue color), in the area between 35°N-37°N. For that reason the information from the satellite is limited there in the highest 500m of the propagated haboob, implying also the existence of much higher values close to the surface.

The second overpass at 7 September 10:35 UTC is actually behind or at the tail of the propagating dust storm (Figure 10a). The thin dust layer that is detected by CALIPSO between 30°N-32°N reaches up to 2 km and maximum dust concentrations of up to 2000-3000 $\mu g\ m^{-3}$ are calculated mostly close to the surface (Figure 10b). Extreme dust concentrations are also found in both satellite and model plots between 34°N-36°N at the tail of the propagating system. Dust values at this area are so high that CALIPSO observation suffers again from total attenuation of the lidar signal after penetrating the first 1000 m and extraordinary concentrations of up to 20000 $\mu g\ m^{-3}$ are found in the lower model levels (up to 1.5 km). Similar values are observed from CALIPSO in the edge of the haboob (33.5°N-34°N) where the signal is strong enough to provide valuable information. The elevated layers (2-4 km) between 36°N-38°N at both CALIPSO and model profiles are dust residuals over the mountains of Turkey. An elevated dust layer of up to 600 $\mu g\ m^{-3}$ is also found south of 35°N in the model at heights between 3-4 km. Due to the aforementioned latency between the true and modeled propagation speeds, the model cross-section is closer to the core of the system hence this layer consists of modeled cyclone uplifted dust that in fact is already west of the CALIPSO track.

3.2.2. Dust load over Cyprus

The observed structure and amounts of dust arriving in Cyprus is described in detail by Mamouri et al. (2016). The arrival of the dust plumes at Limassol in Cyprus is evident in Figure 11. A double layer structure is detected by the lidar at 7 September 19:00 UTC. The relatively shallow dust layer that is found between 0.8-1.7 km with a maximum peak at 2000 $\mu g\ m^{-3}$, comes from the detached dust air mass traveling off the coast of Libanon as described in Section 3.1.1. The model reproduces correctly the height of this layer but the maximum concentration is underestimated by almost 50 %. The upper layer that is detected between 1.8-3.6 km originates from the north part of the fast propagating haboob that catches up with the "Lebanon" dust over Cyprus. The location and dust concentrations of this layer are adequately reproduced by the model. The total modeled dust load is similar to the observed (lidar) dust load but the vertical distribution of dust in two distinct layers is not so clearly reproduced. Model results using the old vegetation database are also shown in Figure 11. As seen by the dashed line in this plot, this simulation failed to reproduce the strength of the event and the maximum concentration is 400 $\mu g\ m^{-3}$ at about 0.7 km height. On the 8th of September the lidar system could not operate due to the extraordinary dust load. The mean MODIS derived AOT on this day varied between 1.5-5 over five sites in Cyprus (Pafos, Limassol, Larnaca, Nicosia, Rizokarpaso), (Mamouri et al., 2016). Given the fact that the maximum retrievable MODIS AOT is 5, these values are most probably an underestimation of the true AOT. The distribution of modeled AOT during 00:00 UTC-15:00 UTC on the 8^{th} of September is shown in Figure12; the dust plume approaches Cyprus from the South and the orographic effect of Mt. Troodos results in an inhomogeneous distribution of dustload over the island, which explains the AOT variability between the sites. The modeled AOT values over the Middle East inland exceed 10 as shown also by the sharp gradient towards the eastern part of Figure 12 plots. However the extreme dust storm affecting Cyprus during the 8^{th} of September is the result of a plume that approaches the island from the south. This dust layer is evident between 1.5-3.5 km in the vertical cross-sections of model dust concentration at 00:00 UTC and 03:00 UTC in Figure 13. Downward mixing of dust as this air mass approaches the topographic barrier of Troodos mountain increases the near-surface concentrations at the southern sites especially during local morning and noon hours (06:00 UTC, 09:00 UTC). In the afternoon hours (12:00 UTC, 15:00 UTC), the development of upward motions over Mt. Troodos separates the dust flow over Cyprus into two distinct cells (a south and a north one) and at this time increased concentrations are found over the northern sites of the island. The maximum simulated concentrations are up to 4000 μg m^{-3} aloft and about 1000 μg m^{-3} close to the surface. Taking into account the complexity of the situation, the spatiotemporal evolution of the episode seems to be correctly explained by the model but the extreme values of 8000-10000 mg m^{-3} that are reported by Mamouri et al. (2016) are not reproduced. This discrepancy can be attributed to a variety of reasons related to both dust and atmospheric properties that are not properly resolved even at this fine model scale (e.g. more intense downward mixing or increased emissions from the sources). The modeled versus observed maximum AOT values for the five sites are also shown in Table 1. The model reproduces the higher AOTs at the most southern sites (Limassol and Pafos) compared to the central and north sites. Following the previous discussion about the already underestimated MODIS AOT it seems that the model reproduces the distribution of dust over Cyprus however with an overall underestimation of more than 2. A possible explanation could be also that the dry river beds of Tigris and Euphrates as well as several dust sources over Syria and North Iraq provide even more erodible sediments than those assumed by the model hence the discrepancies in dust concentrations.

Table 1. Maximum MODIS and RAMS AOT over Cyprus 8 September 2015

	Pafos	Limassol	Larnaca	Nicosia	Rizokarpaso
$MODIS_{AOT}$	3.5	5.0	5.0	2.0	5.0
$RAMS_{AOT}$	3.5	4.0	3.0	3.0	3.0

4. Discussion and Conclusions

A combination of meteorological and landuse conditions resulted in the formation of an unprecedented dust episode over Middle East and East Mediterranean during 6-11 September 2015. This event is unique due to the coincidence of various atmospheric phenomena related with the generation of turbulence and dust production. Interpretation and analysis of remote sensing data (EARLINET, CALIPSO, MSG-SEVIRI) and modeling simulations (RAMS-ICLAMS) reveals the main reasons that led in the uplift and persistence of the dust layers. The major processes affecting the generation of the dust storm are found to be:

1. The formation of a strong thermal low over Syria that lifted dust up to 4 km.
2. The intrusion of a moist and unstable air mass from the Arabian Sea that triggered convective activity over Iraq-Iran-Syria-Turkey borderline.
3. The generated outflow boundaries that led in dust deflation and formed a westward propagating haboob merging with the previously elevated dust over Syria.
4. The efficiency of Middle East dust sources is increased as an aftermath of war and the related changes in land use.

As reported by Mamouri et al. (2016), almost all operational dust models failed to forecast this event. RAMS-ICLAMS in this study is not used in forecasting mode but rather as a tool for the a-posteriori analysis and explanation of the event. This means that the configuration of several model parameters such as the nested grid structure, convective parameterization schemes, dust source strength etc. is guided by the available observations. In this context, most observed processes are successfully described by the model and the various physical mechanisms that took place during the event are explained. However, certain inaccuracies in the quantification of atmospheric variables and spatiotemporal deviations in the description of convection and other physical processes can still significantly decrease the model skill especially regarding the quantification of dust mass profiles.

The analysis presented here raises considerations regarding the forecast skills of the atmospheric dust models, since even though such extreme episodes are very seldom they still represent the most threatening dust hazards. The long range transport and the general circulation of dust in the atmosphere are nowadays adequately forecasted by most global models but convectively driven episodes cannot be resolved at synoptic and mesoscale resolutions. Moreover, a recent study by Pope et al. 2016 suggests that unresolved haboobs may be responsible for up to 30% of the total atmospheric dust and such considerations raise questions on the current status of early warning systems for dust episodes. It is probably obvious that such a system cannot rely exclusively on modeling simulations. As shown at the present study, the complexity of these events makes their forecast very challenging and even at convection permitting resolutions, it is possible that a certain model configuration could successfully reproduce a specific event but not all similar events. Moreover, such high resolution grid-space can only be applied over limited areas due to restrictions in computational power.

Remote sensing observations can play an important role for the provision of more accurate dust forecasts. Engagement of geostationary satellite observations (MSG, Sentinel-4) and CALIPSO profiles in forecasting activities could improve the forecasting skill either by the direct assimilation of satellite data in dust models or by issuing human-assisted early warnings. Expansion of a lidar network close to dust source areas (e.g. Sahara, Middle East) will also complement model activities through the provision of ground truth observations for the vertical profile of dust plumes. Additionally, the activation of synchronous observations from the EARLINET network following a dust forecast notice will allow a closer investigation of the physical processes that drive these events

.

Acknowledgements

The authors acknowledge support through the following projects and research programs: BEYOND under grant agreement no. 316210 of the European Union Seventh Framework Programme FP7-REGPOT-2012-2013-1. ACTRIS-2 under grant agreement no. 654109 of the European Union's Horizon 2020 research and innovation programme. ECARS under grant agreement No 602014 from the European Union's Horizon 2020 Research and Innovation programme. MarcoPolo under grant agreement no. 606953 of the European Union Seventh Framework Programme FP7/2007-2013. The authors acknowledge EARLINET for providing aerosol lidar profiles available under the World Data Center for Climate (WDCC) (The EARLINET publishing group 2000-2010, 2014a. CALIPSO data were obtained from the ICARE Data Center (http://www.icare.univ-lille1.fr/) and from the NASA Langley Research Center Atmospheric Science Data Center. CALIPSO data were provided by NASA. We thank the ICARE Data and Services Center for providing access to the data used in this study and their computational center.

References

Ansmann A., Tesche, M., Knipperts, P., Bierwirth, E., Althausen, D., Muller, D. and Schulz. O.: Vertical profiling of convective dust plumes in southern Morocco during SAMUM. Tellus 61B, doi:10.1111/j.1600-0889.2008.00384.x., 2009

Ansmann, A., Petzold, A., Kandler, K., Tegen, I., Wendisch, M., Müller, D., Weinzierl, B., Müller, T., and Heintzenberg, J.: Saharan Mineral Dust Experiments SAMUM-1 and SAMUM-2: what have we learned?, Tellus, 63B, 403–429, 2011

Ansmann, A., Seifert, P., Tesche, M., and Wandinger, U.: Profiling of fine and coarse particle mass: case studies of Saharan dust and Eyjafjallajökull/Grimsvötn volcanic plumes, Atmos. Chem. Phys., 12, 9399–9415, doi:10.5194/acp-12-9399-2012, 2012.

Barahona, D., West, R. E. L., Stier, P., Romakkaniemi, S., Kokkola, H., and Nenes, A.: Comprehensively accounting for the effect of giant CCN in cloud activation parameterizations, Atmos. Chem. Phys., 10, 2467–2473, doi:10.5194/acp-10-2467-2010, 2010.

Benedetti A., J.-J., Morcrette, O. Boucher, A. Dethof, R. J. Engelen, M. Fisher, H. Flentje, N. Huneeus, L. Jones, J. W. Kaiser, S. Kinne, A. Mangold, M. Razinger, A. J. Simmons, and M. Suttie: Aerosol analysis and forecast in the European Centre for Medium-Range Weather Forecasts Integrated Forecast System: 2. Data assimilation, J. Geophys. Res., 114, D13205, doi:10.1029/2008JD011115., 2009

Bou Karam, D., Flamant, C., Knippertz, P., Reitebuch, O., Pelon, J., Chong, M., and Dabas, A: Dust emissions over the Sahel associated with the West African Monsoon inter-tropical discontinuity region: a representative case study, Q. J. Roy. Meteor. Soc., 134, 621–634, 2008.

Cook, B. I., Anchukaitis, K. J., Touchan, R., Meko, D. M. and Cook, E. R.: Spatiotemporal drought variability in the Mediterranean over the last 900 years, J. Geophys. Res. Atmos., 121(5), 2015JD023929, doi:10.1002/2015JD023929, 2016.

Cotton W. R., Pielke Sr., R. A., Walko, R. L., Liston, G. E., Tremback, C. J., Jiang, H., McAnelly, R. L., Harrington, J. Y., Nicholls, M. E., Carrio, G. G., and McFadden, J. P.: RAMS 2001: Current status and future directions, Meteor. Atmos. Phys., 82, 5–29, 2003

DeFries, R. S. and Townshend, J. R. G.: NDVI-derived land cover classifications at a global scale, International Journal of Remote Sensing, 15(17), 3567–3586, doi:10.1080/01431169408954345, 1994.

Didan, K: MOD13A3 MODIS/Terra vegetation Indices Monthly L3 Global 1km SIN Grid V006, , doi:10.5067/MODIS/MOD13A3.006, 2015.

Emmel C, Knippertz P, Schulz O (2010) Climatology of convective density currents in the southern foothills of the Atlas mountains. J Geophys Res 115, D11115. doi:10.1029/2009JD011819

Fountoukis, C., Nenes, A., Meskhidze, N., Bahreini,, R., Conant, W. C., Jonsson, H., Murphy, S., Sorooshian, A., Varutbangkul, V., Brechtel, F., Flagan, R. C., and Seinfeld, J. H.: Aerosol – cloud drop concentration closure for clouds sampled during the International Consortium for Atmospheric Research on Transport and Transformation 2004 campaign, J. Geophys. Res., 112, D10S30, doi:10.1029/2006JD007272, 2007.

Ginoux, P., Prospero, J. M., Gill, T. E., Hsu, N. C. and Zhao, M.: Global-scale attribution of anthropogenic and natural dust sources and their emission rates based on MODIS Deep Blue aerosol products, Rev. Geophys., 50(3), RG3005, doi:10.1029/2012RG000388, 2012.

Gong, S. L., Barrie, L. A., and Lazare, M.: Canadian Aerosol Module (CAM): a size-segregated simulation of atmospheric aerosol processes for climate and air quality models. 2. Global seasalt aerosol and its budgets, J. Geophys. Res., 107(D24), 4779, doi:10.1029/2001JD002004, 2002.

Gong, S. L.: A parameterization of sea-salt aerosol source function for sub- and super-micron particles, Global Biogeochem. Cy., 17, 1097, doi:10.1029/2003GB002079, 2003.

Iacono, M. J., Mlawer, E. J., Clough, S. A., and Morcrette, J. J.: Impact of an improved longwave radiation model, RRTM, on the energy budget and thermodynamic properties of the NCAR Community Climate Model, CCM3, J. Geophys. Res., 105, 14873– 14890, 2000

Jaafar, H. H. and Woertz, E.: Agriculture as a funding source of ISIS: A GIS and remote sensing analysis, Food Policy, 64, 14–25, doi:10.1016/j.foodpol.2016.09.002, 2016.

Kain, J. S. and Fritsch, J. M.: Convective parameterization for mesoscale models: The Kain-Fritsch scheme. The representation of cumulus convection in numerical models, Meteor. Monogr., No. 24, Amer. Meteor. Soc., 165–170, 1993.

Knippertz P, Trentmann J. Seifert A., High resolution simulations of convective cold pools over the northwestern Sahara. J. Geophys. Res. 2009; 114:D21109. doi: 10.1029/2007JD008774., 2009

Leeuw, G., Neele, F. P., Hill, M., Smith, M. H., and Vignali, E.: Production of sea spray aerosol in the surf zone, J. Geophys. Res.- Atmos., 105, 29397–29409, 2000.

Lensky I.M. and D. Rosenfeld, 2008: Clouds-Aerosols-Precipitation Satellite Analysis Tool (CAPSAT). Atmos. Chem. Phys., 8, 6739–6753.

Mamouri, R. E., Ansmann, A., Nisantzi, A., Kokkalis, P., Schwarz, A., and Hadjimitsis, D.: Low Arabian dust extinctionto-backscatter ratio, Geophys. Res. Lett., 40, 4762–4766,doi:10.1002/grl.50898, 2013.

Mamouri R.E., Ansmann, A., Nisantzi, A., Solomos, S., Kallos, G., and Hadjimitsis, D.G.: Extreme dust storm over the eastern Mediterranean in September 2015: satellite, lidar, and surface observations in the Cyprus region Atmos. Chem. Phys., 16, 1–14, 2016 www.atmos-chem-phys.net/16/1/2016/doi:10.5194/acp-16-1-2016.

Mamouri, R.E. and Ansmann, A.: Fine and coarse dust separation with polarization lidar: Extended Methodology for multiple wavelengths, to be submitted to ACP, 2017.

Marsham, J. H., N. S. Dixon, L. Garcia-Carreras, G. M. S. Lister, D. J. Parker, P. Knippertz, and C. E. Birch : The role of moist convection in the West African monsoon system: Insights from continental-scale convection-permitting simulations, Geophys. Res. Lett., 40, 1843–1849, doi:10.1002/grl.50347., 2013

Marticorena, B. and Bergametti, G.: Modeling the atmospheric dust cycle: 1. Design of a soil derived dust emission scheme, J. Geophys. Res., 100, 16415–16430, 1995.

Meyers, M. P., Walko, R. L., Harrington, J. Y., and Cotton, W. R: New RAMS cloud microphysics parameterization. Part II: The two-moment scheme, Atmos. Res., 45, 3–39, 1997

Mlawer, E. J., Taubman, S. J., Brown, P. D., Iacono, M. J., and Clough, S. A.: Radiative transfer for inhomogeneous atmospheres: RRTM, a validated correlated-k model for the longwave, J. Geophys. Res., 102(D14), 16663–16682, 1997.

Monahan, E. C., Spiel, D. E., and Davidson, K. L.: A model of marine aerosol generation via whitecaps and wave disruption, in: Oceanic Whitecaps, edited by: Monahan, E. C. and Mac Niocaill, G., D. Reidel, 167–174, 1986.

Notaro, M., Yu, Y. and Kalashnikova, O. V.: Regime shift in Arabian dust activity, triggered by persistent Fertile Crescent drought, J. Geophys. Res. Atmos., 120(19), 2015JD023855, doi:10.1002/2015JD023855, 2015.

Pielke, R. A., Cotton, W. R., Walko, R. L., Tremback, C. J., Lyons, W. A., Grasso, L. D., Nicholls, M. E., Moran, M. D., Wesley, D. A., Lee, T. J., and Copeland, J. H.: A comprehensive meteorological modeling system – RAMS, Meteorol. Atmos. Phys., 49, 69–91, 1992.

Pope, R. J., J. H. Marsham, P. Knippertz, M. E. Brooks, and A. J. Roberts: Identifying errors in dust models from data assimilation, Geophys. Res. Lett., 43, 9270–9279, doi:10.1002/2016GL070621., 2016

Prospero, J. M., Ginoux, P., Torres, O., Nicholson, S. E. and Gill, T. E.: Environmental Characterization of Global Sources of Atmospheric Soil Dust Identified with the Nimbus 7 Total Ozone Mapping Spectrometer (toms) Absorbing Aerosol Product, Rev. Geophys., 40(1), 1002, doi:10.1029/2000RG000095, 2002.

Reinfried, F., I. Tegen, B. Heinold, O. Hellmuth, K. Schepanski, U. Cubasch, H. Huebener, and P. Knippertz : Simulations of convectively-driven density currents in the Atlas region using a regional model: Impacts on dust emission and sensitivity to horizontal resolution and convection schemes, J. Geophys. Res., 114, D08127, doi:10.1029/2008JD010844., 2009

Roberts, A. J., P. Knippertz : The formation of a large summertime Saharan dust plume: Convective and synoptic-scale analysis, J. Geophys. Res. Atmos., 119, 1766–1785, doi:10.1002/2013JD020667., 2014

Ryder, C. L., McQuaid, J. B., Flamant, C., Rosenberg, P. D., Washington, R., Brindley, H. E., Highwood, E. J., Marsham, J. H., Parker, D. J., Todd, M. C., Banks, J. R., Brooke, J. K., Engelstaedter, S., Estelles, V., Formenti, P., Garcia-Carreras, L., Kocha, C., Marenco, F., Sodemann, H., Allen, C. J. T., Bourdon, A., Bart, M., Cavazos-Guerra, C., Chevaillier, S., Crosier, J., Darbyshire, E., Dean, A. R., Dorsey, J. R., Kent, J., O'Sullivan, D., Schepanski, K., Szpek, K., Trembath, J., and Woolley, A.: Advances in understanding mineral dust and boundary layer processes over the Sahara from Fennec aircraft observations, Atmos. Chem. Phys., 15, 8479–8520, doi:10.5194/acp-15-8479- 2015, 2015

Schepanski, K., Tegen, I., Todd, M. C., Heinold, B., Bonisch, G., Laurent, B., and Macke, A.: Meteorological processes forcing Saharan dust emission inferred from MSG-SEVIRI observations of subdaily dust source activation and numerical models, J. Geophys. Res., 114, D10201, doi:10.1029/2008JD010325, 2009.

Seinfeld, J. H. and Pandis, S. N.: Atmospheric Chemistry and Physics: From Air Pollution to Climate Change, J. Wiley, New York, 1998

Solomos, S., Kallos, G., Kushta, J., Astitha, M., Tremback, C., Nenes, A., and Levin, Z.: An integrated modeling study on the effects of mineral dust and sea salt particles on clouds and precipitation, Atmos. Chem. Phys., 11, 873–892, doi:10.5194/acp- 11-873-2011, 2011

Solomos, S., Kallos, G., Mavromatidis, E., and Kushta, J.: Density currents as a desert dust mobilization mechanism, Atmos. Chem. Phys., 12, 11199-11211, doi:10.5194/acp-12-11199-2012, 2012.

Spyrou, C., Mitsakou, C., Kallos, G., Louka, P., and Vlastou, G.: An improved limited-area model for describing the dust cycle in the atmosphere, J. Geophys. Res., 115, D17211, doi:10.1029/2009JD013682, 2010.

Takemi, T.: Explicit simulations of convective-scale transport of mineral dust in severe convective weather, J. Meteorol. Soc. Jpn., 83A, 187–203, 2005.

Takemi, T.: Structure and evolution of a severe squall line over the arid region in Northwest China. Mon. Wea. Rev., 127, 1301–1309., 1999.

The EARLINET publishing group 2000–2010: Adam, M., Alados-Arboledas, L., Althausen, D., Amiridis, V., Amodeo, A., Ansmann, A., Apituley, A., Arshinov, Y., Balis, D., Belegante, L., Bobrovnikov, S., Boselli, A., Bravo-Aranda, J. A., Bösenberg, J., Carstea, E., Chaikovsky, A., Comerón, A., D'Amico, G., Daou, D., Dreischuh, T., Engelmann, R., Finger, F., Freudenthaler, V., Garcia-Vizcaino, D., García, A. J. F., Geiß, A., Giannakaki, E., Giehl, H., Giunta, A., de Graaf, M., Grana-dos-Muñoz, M. J., Grein, M., Grigorov, I., Groß, S., ruening, C., Guerrero-Rascado, J. L., Haeffelin, M., Hayek, T., Iarlori, M., Kanitz, T., Kokkalis, P., Linné, H., Madonna, F., Mamouri , R.-E., Matthias, V., Mattis, I., Menéndez, F. M., Mitev, V., Mona, L., Morille, Y., Muñoz, C., Müller, A., Müller, D., Navas-Guzmán, F., Nemuc, A., Nicolae, D., Pandolfi, M., Papayannis, A., Pappalardo, G., Pelon, J., Perrone, M. R., Pietruczuk, A., Pisani, G., Potma, C., Preißler, J., Pujadas, M., Putaud, J., Radu, C., Ravetta, F., Reigert, A., Rizi, V., Rocadenbosch, F., Rodríguez, A., Sauvage, L., Schmidt, J., Schnell, F., Schwarz, A., Seifert, P., Serikov, I., Sicard, M., Silva, A. M., Simeonov, V., Siomos, N., Sirch, T., Spinelli, N., Stoyanov, D., Talianu, C., Tesche, M., De Tomasi, F., Trickl, T., Vaughan, G., Volten, H., Wagner, F., Wandinger, U., Wang, X., Wiegner, M., and Wilson, K. M.: EARLINET all observations (2000–2010), World Data Center for Climate (WDCC), doi:10.1594/WDCC/EN_all_measurements_2000-2010, 2014a.

Voss, K. A., Famiglietti, J. S., Lo, M., de Linage, C., Rodell, M. and Swenson, S. C.: Groundwater depletion in the Middle East from GRACE with implications for transboundary water management in the Tigris-Euphrates-Western Iran region, Water Resour. Res., 49(2), 904–914, doi:10.1002/wrcr.20078, 2013.

Vukovic, A., Vujadinovic, M., Pejanovic, G., Andric, J., Kumjian, M. R., Djurdjevic, V., Dacic, M., Prasad, A. K., El-Askary, H. M., Paris, B. C., Petkovic, S., Nickovic, S., and Sprigg, W. A.: Numerical simulation of "an American haboob", Atmos. Chem. Phys., 14, 3211-3230, doi:10.5194/acp-14-3211-2014, 2014.

Zhang, K. M., Knipping, E. M., Wexler, A. S., Bhave, P. V., and Tonnesen, G. S.: Size distribution of sea-salt emissions as a function of relative humidity, Atmos. Environ., 39, 3373–3379, 2005.

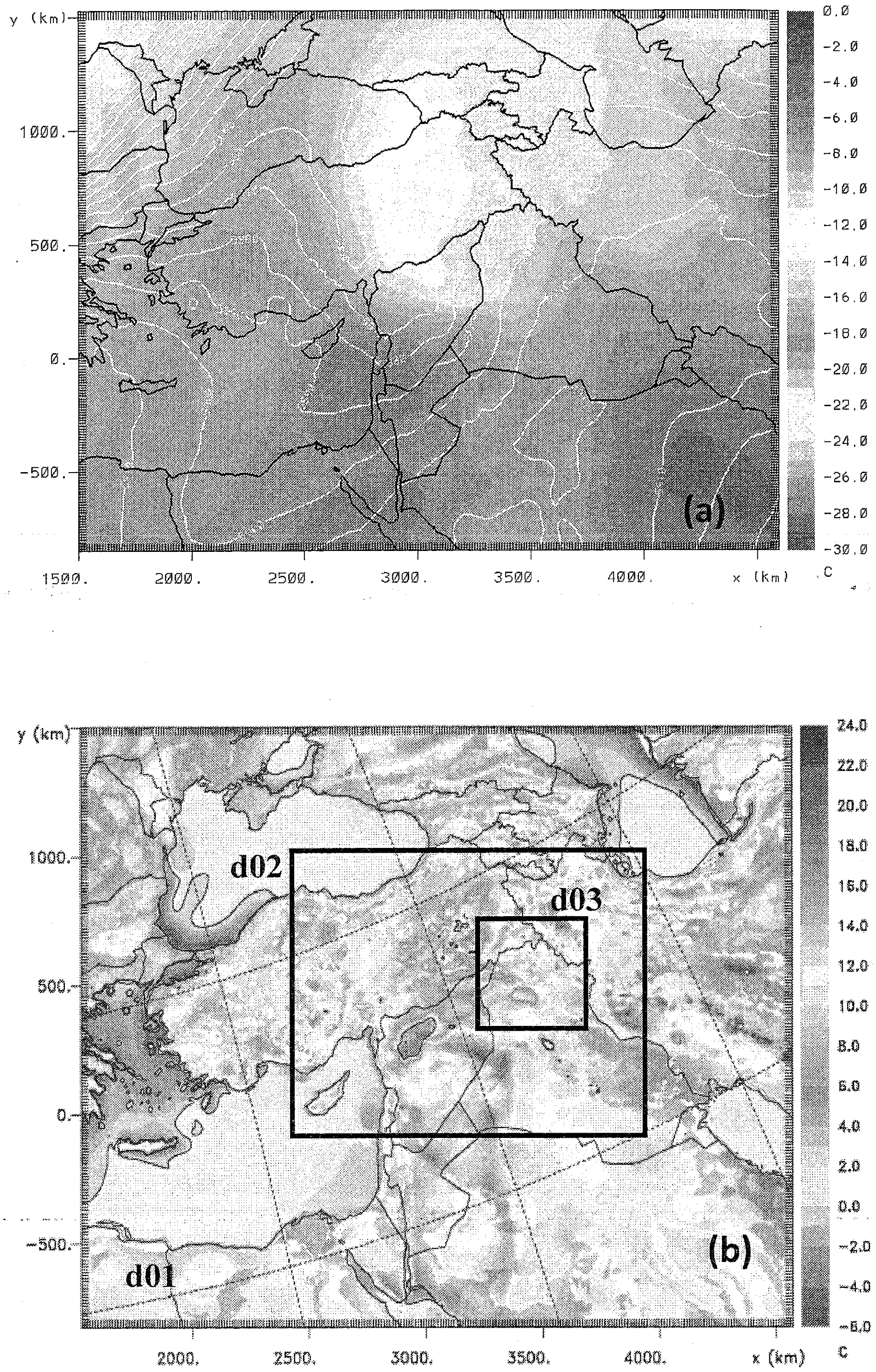

Figure 1. a) Model geopotential height contours (every 10 m) and temperature (color scale in °C) at 500mb, 6 September 2015, 00:00 UTC; b) Difference (°C) between model soil temperature and model temperature at 2m, 10:00 UTC, 6 September 2015. Black rectangulars indicate the location of the nested model domains (d01:12×12 km, d02:4×4 km, d03:2×2 km).

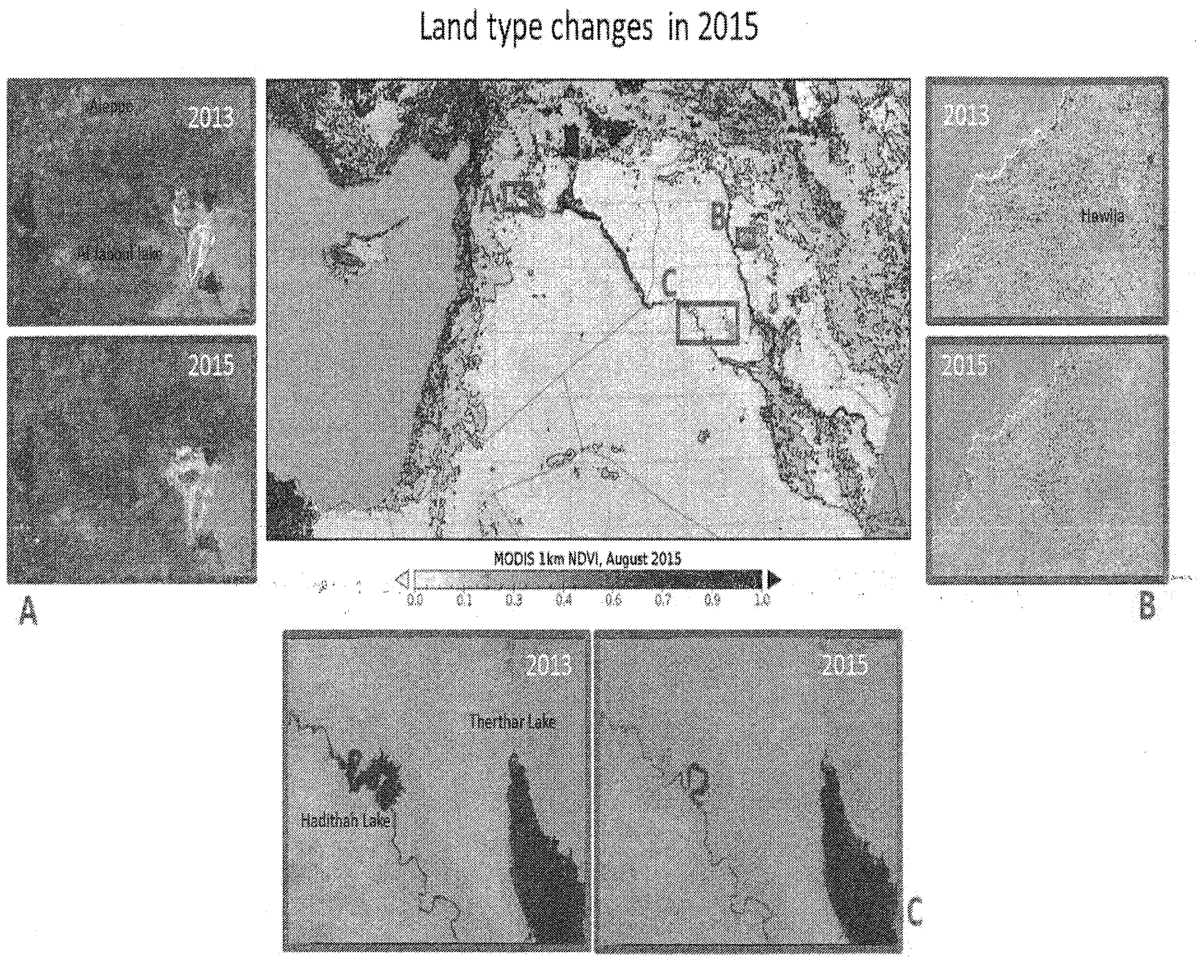

Figure 2. (central panel) MODIS NDVI observations for August 2015 were used to identify regions of bare soil that can be sources of dust aerosols. The contour lines correspond to the major ticks of the color scale. Large regions of wester Syria and Iraq have NDVI values from 0 to 0.1. The three subpanels show examples of land type change between summer 2013 and summer 2015. (Subpanel A) Landsat 8 natural color images of Aleppo region, Syria shows changes of cultivation patterns and drying of nearby Al Jaboul lake (e.g. the bright areas of the Al Jaboul Lake - dry parts of the lake - increased from 2013 to 2015); (Subpanel B) Landsat 8 NDVI index images in the region of Hawija, Kirkuk Province, Iraq reveal that large areas remained uncultivated in 2015 (e.g. the 2013 map shows many more green spots - agriculturally used areas - than the 2015 map); (Subpanel C) Landsat 8 natural color images showing diminishing area of Haditah Lake on the Euphrates river and the drying up of the Therthar canal and lake.

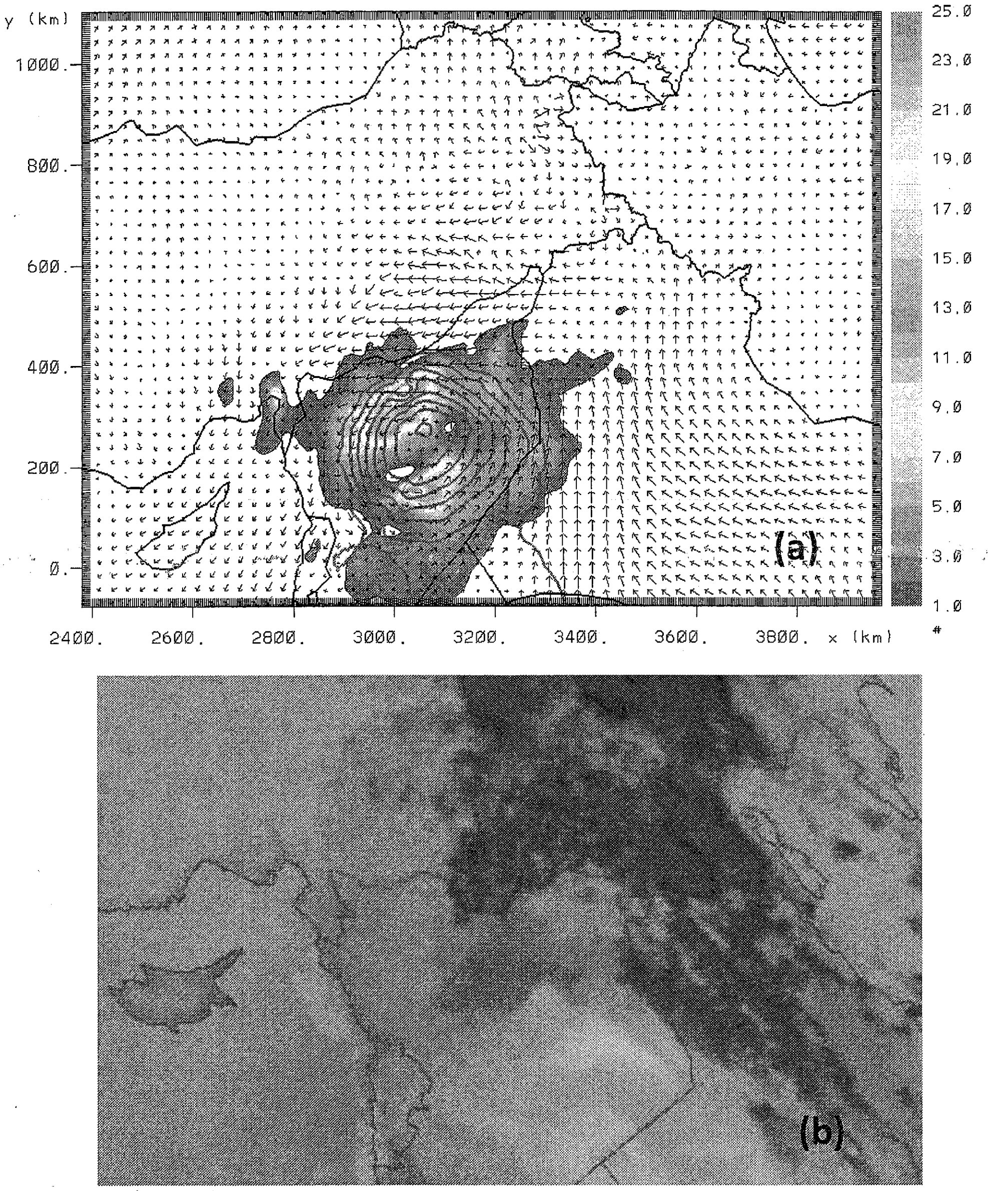

Figure 3. a) Model AOD (color scale) , geopotential height at 850 mb (red contours from 1490 to 1505 m every 2.5 m) and wind vectors at 850mb ; b) MSG SEVIRI dust RGB at 08:00 UTC, 6 September 2015

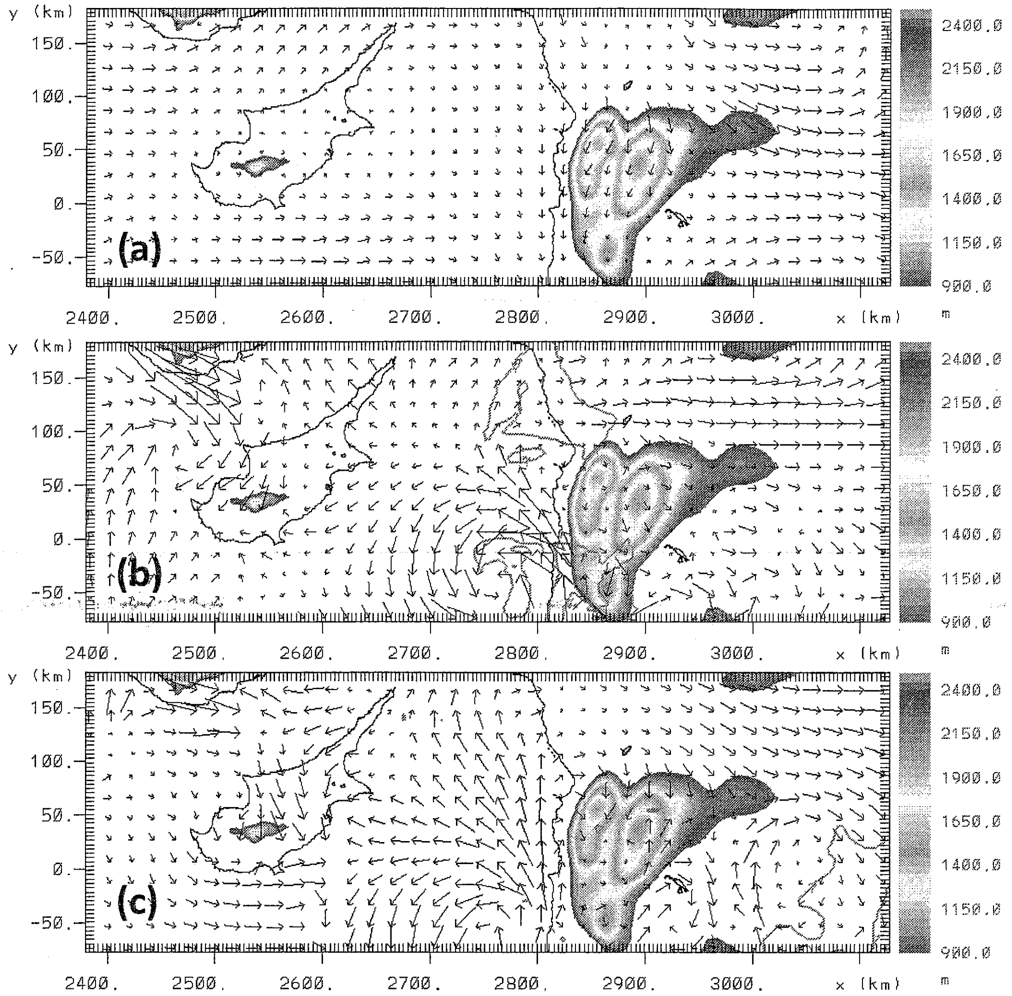

Figure 4. Model topography (color scale), wind vectors at the first model layer (50 m) and cloud fraction > 70% (red contour), zoom from the second model grid, 6 September 2015, 00:00, 06:00, 12:00 UTC.

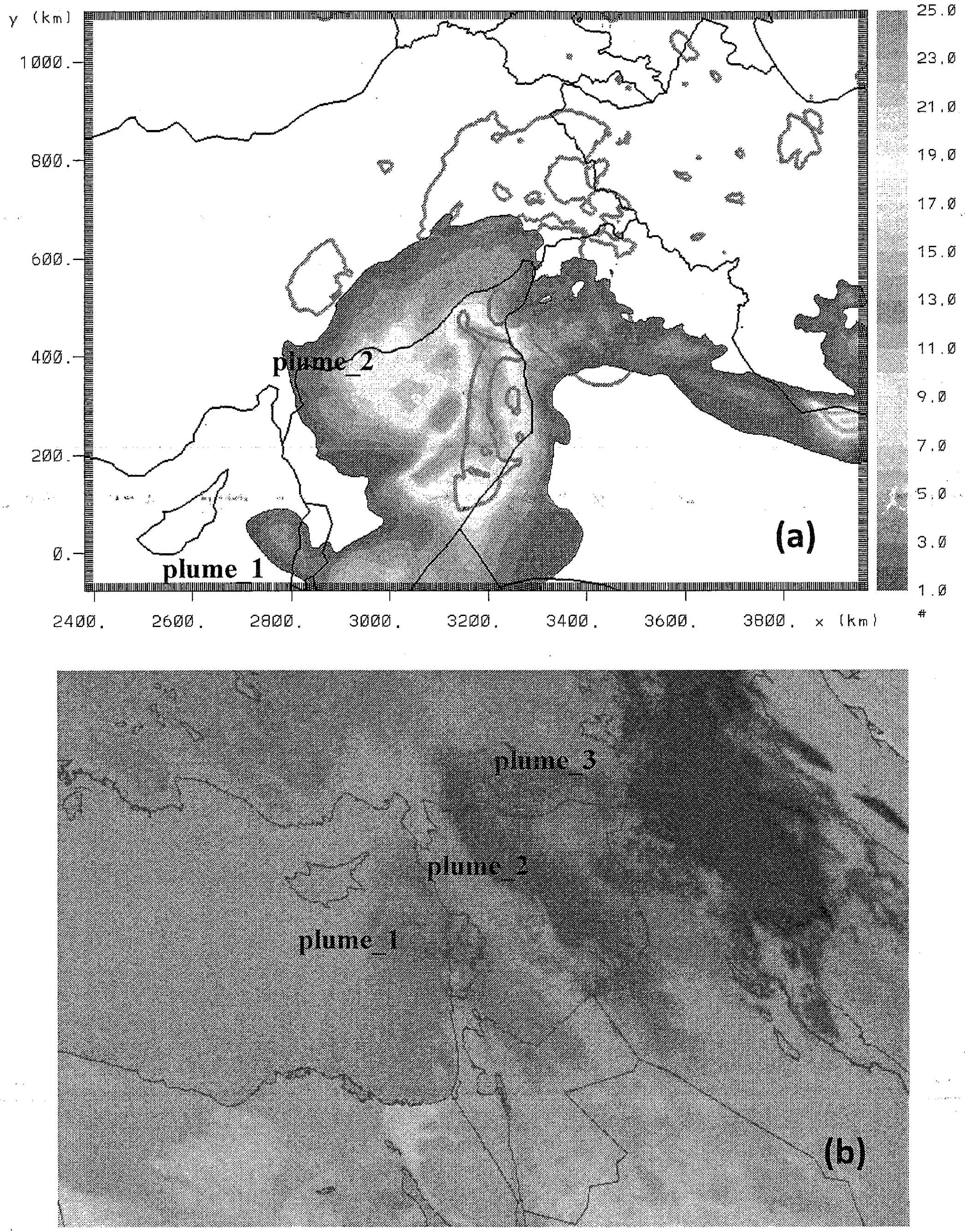

Figure 5. a) Model AOD at 550 nm (color scale) and cloud cover > 70% (red contour). b) MSG-SEVIRI dust RGB component, 7 September 2015, 00:00 UTC

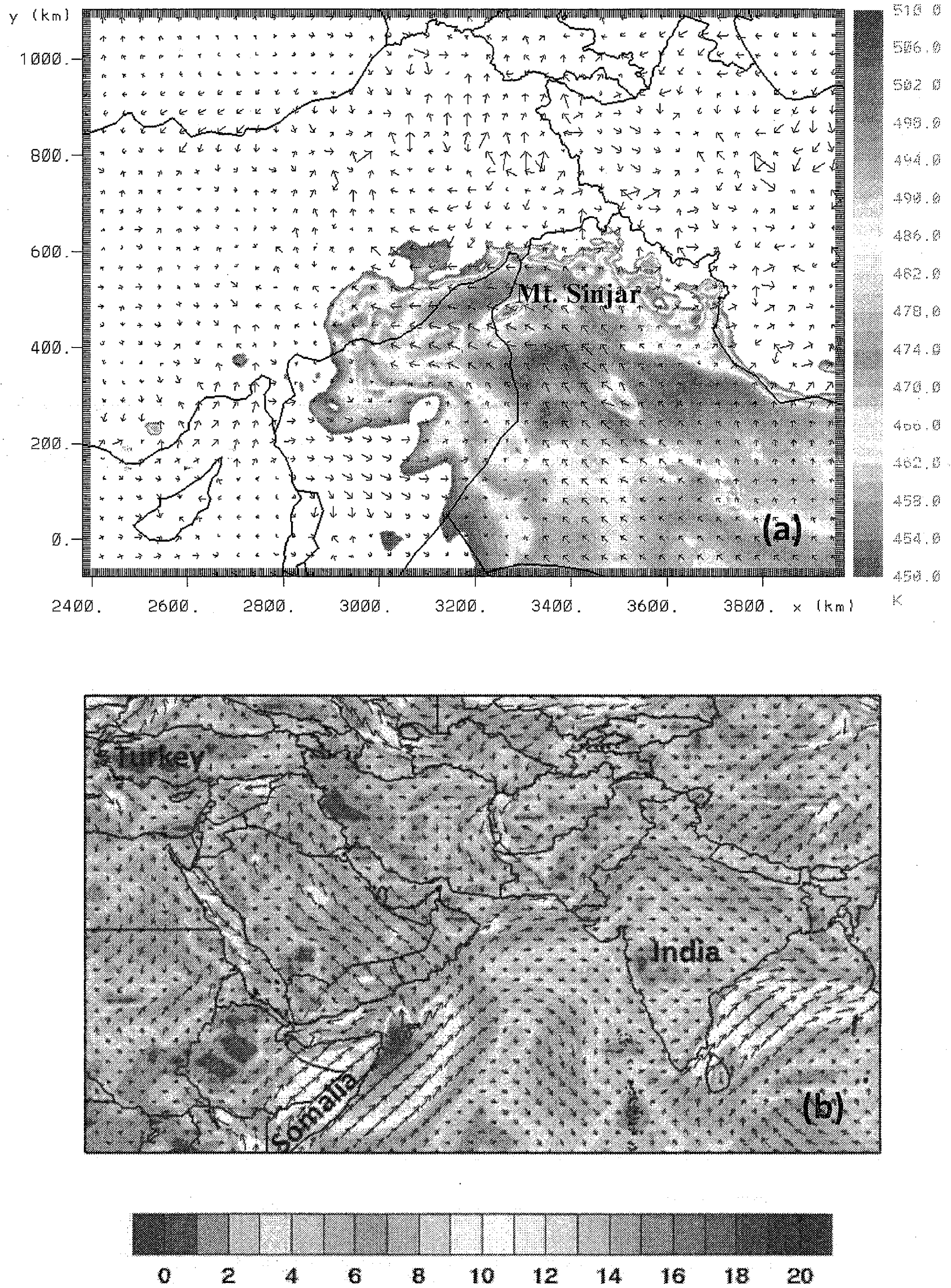

Figure 6. a) Model equivalent potential temperature (K) and wind vectors at 50m above ground, 6 September 2015, 13:00 UTC. b) Wind speed at 10m from the NCEP final analysis (FNL) dataset, 6 September 2015, 06:00 UTC.

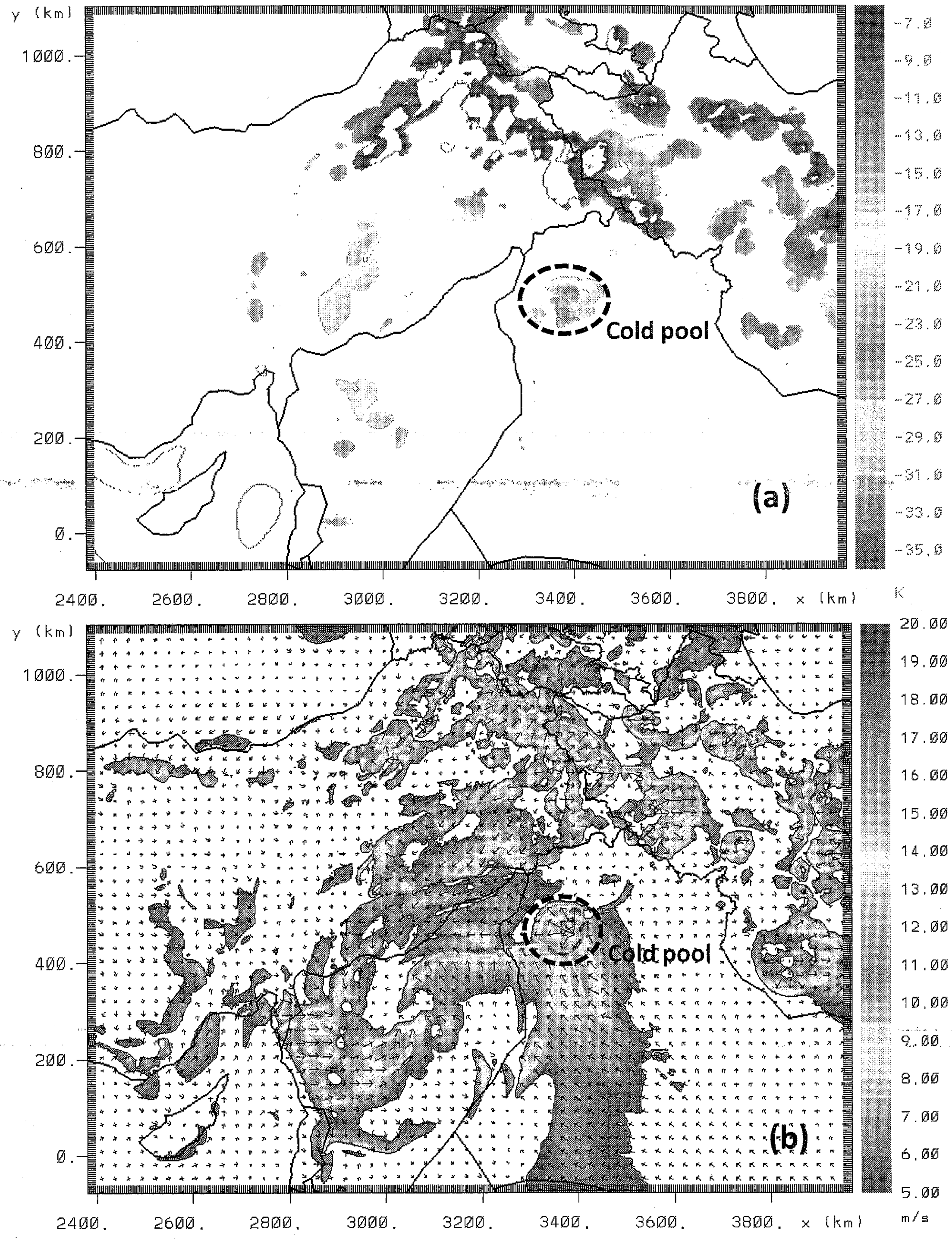

Figure 7. a) Model rain droplets – air temperature difference in K. b) Model wind speed at 10m (ms^{-1}), 6 September 2015, 15:00 UTC. The dashed line denotes the location of the cold pool.

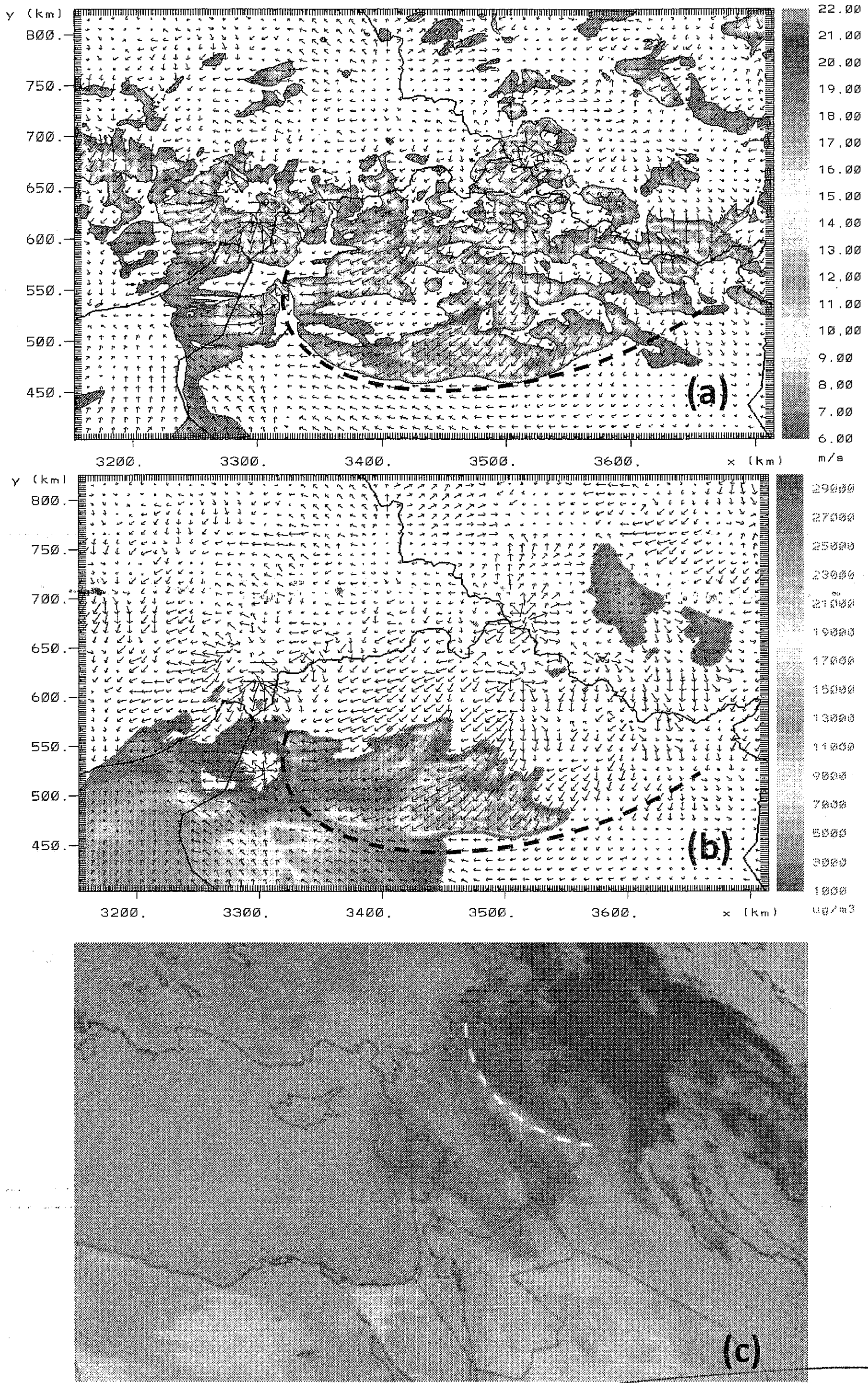

Figure 8. a) Model wind speed greater that 6 ms^{-1} at 10m and b) Near surface model dust concentration (μg m^{-3}) from the inner grid (2×2km) c) MSG-SEVIRI RGB component, 6 September 2015, 20:00 UTC. The dashed lines indicates the haboob front location.

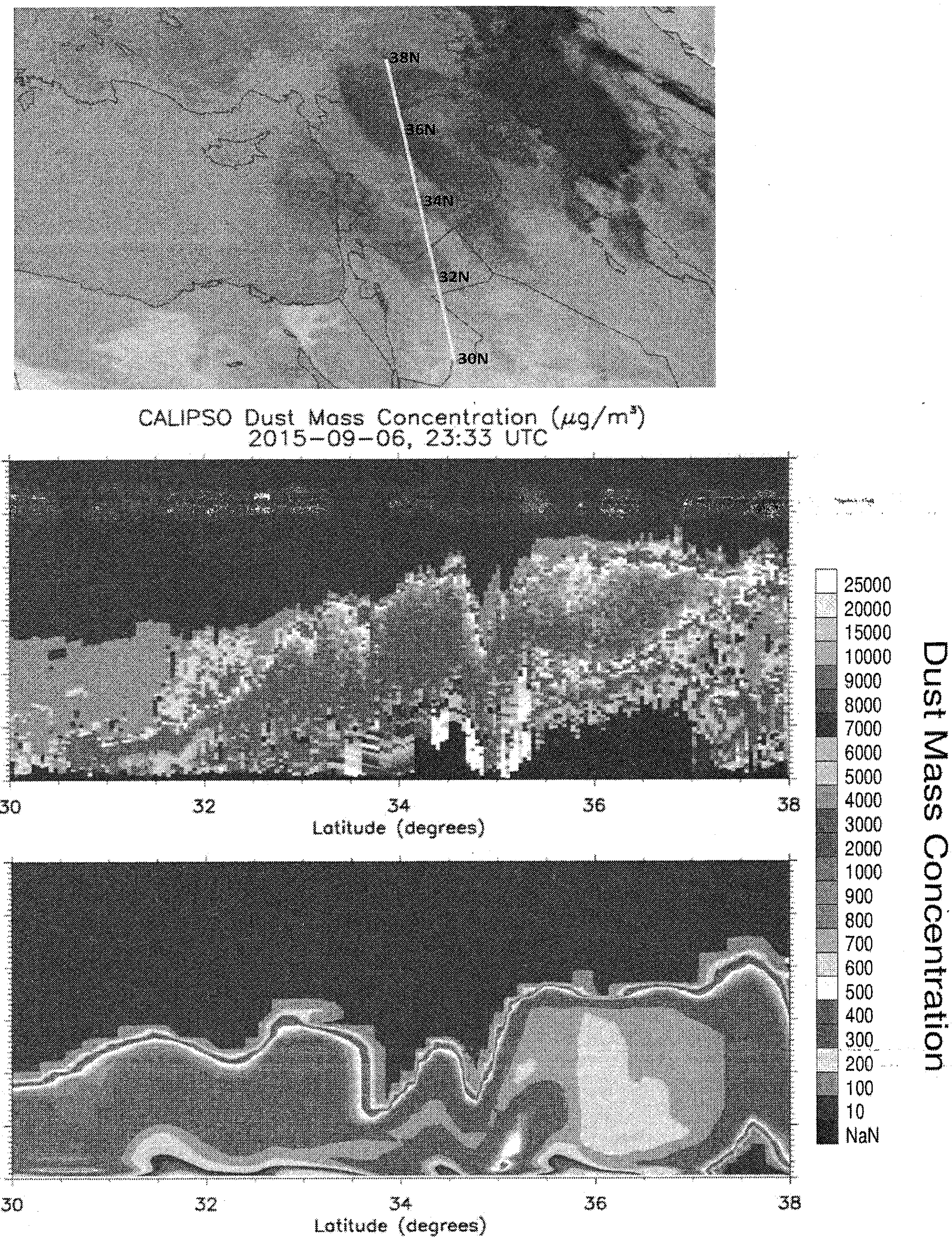

Figure 9. a) MSG-SEVIRI RGB map and CALIPSO overflight (green line), b) CALIPSO dust mass concentration (μg m^{-3}) and c) model dust mass concentration at 6 September 2015, 23:33 UTC. Due to the severity of the event CALIPSO signal is totally attenuated bellow ~1km a.s.e. in the area between 35-37°N (dark blue color).

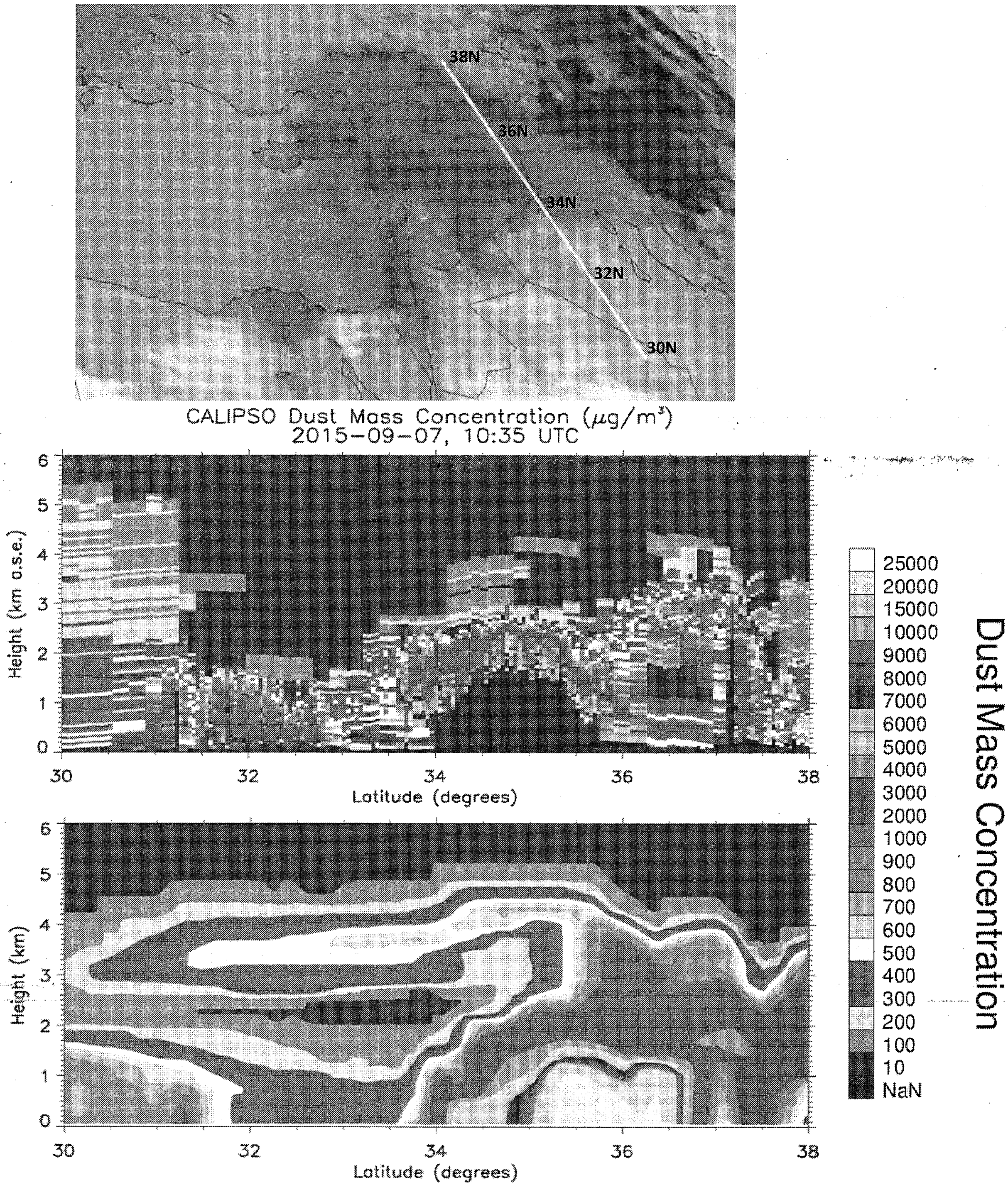

Figure 10. a) MSG-SEVIRI RGB map and CALIPSO overflight (green line), b) CALIPSO dust mass concentration (μg m^{-3}) and c) model dust mass concentration at 7 September 2015, 10:35 UTC. Due to the severity of the event CALIPSO signal is totally attenuated bellow ~1km a.s.e. in the area between 34-36°N (dark blue color).

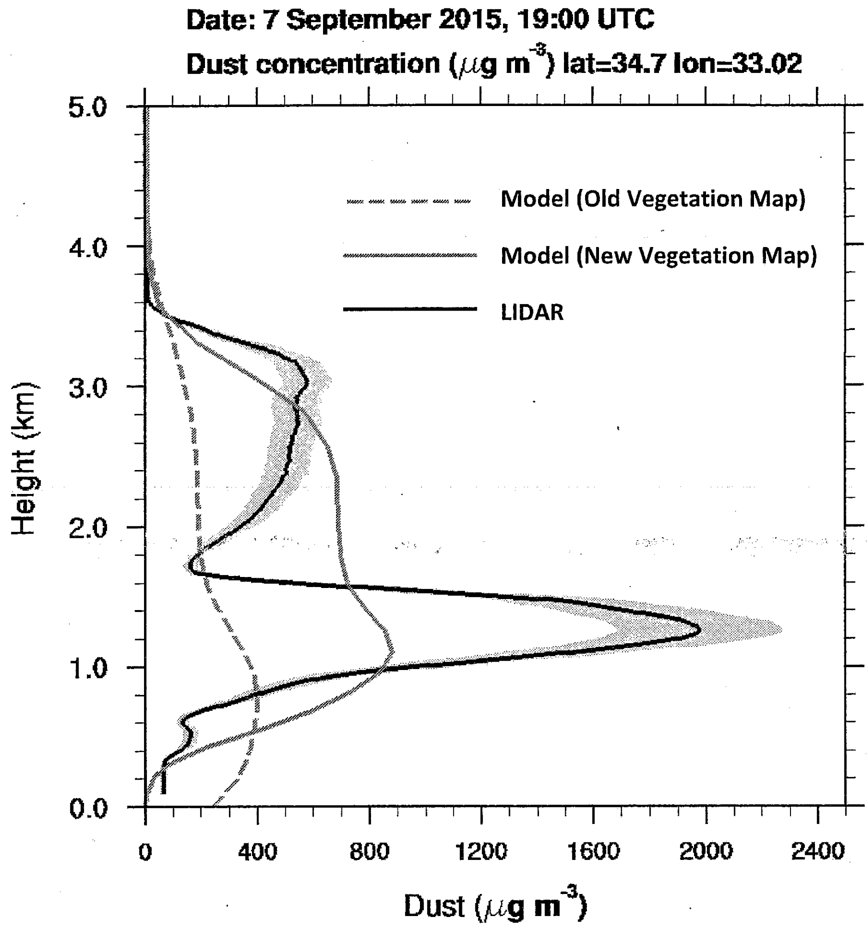

Figure 11. Vertical profile of dust concentration on 7 September 19:00 UTC over Limassol. Blue shadow indicates a 20% uncertainty of the lidar measurements.

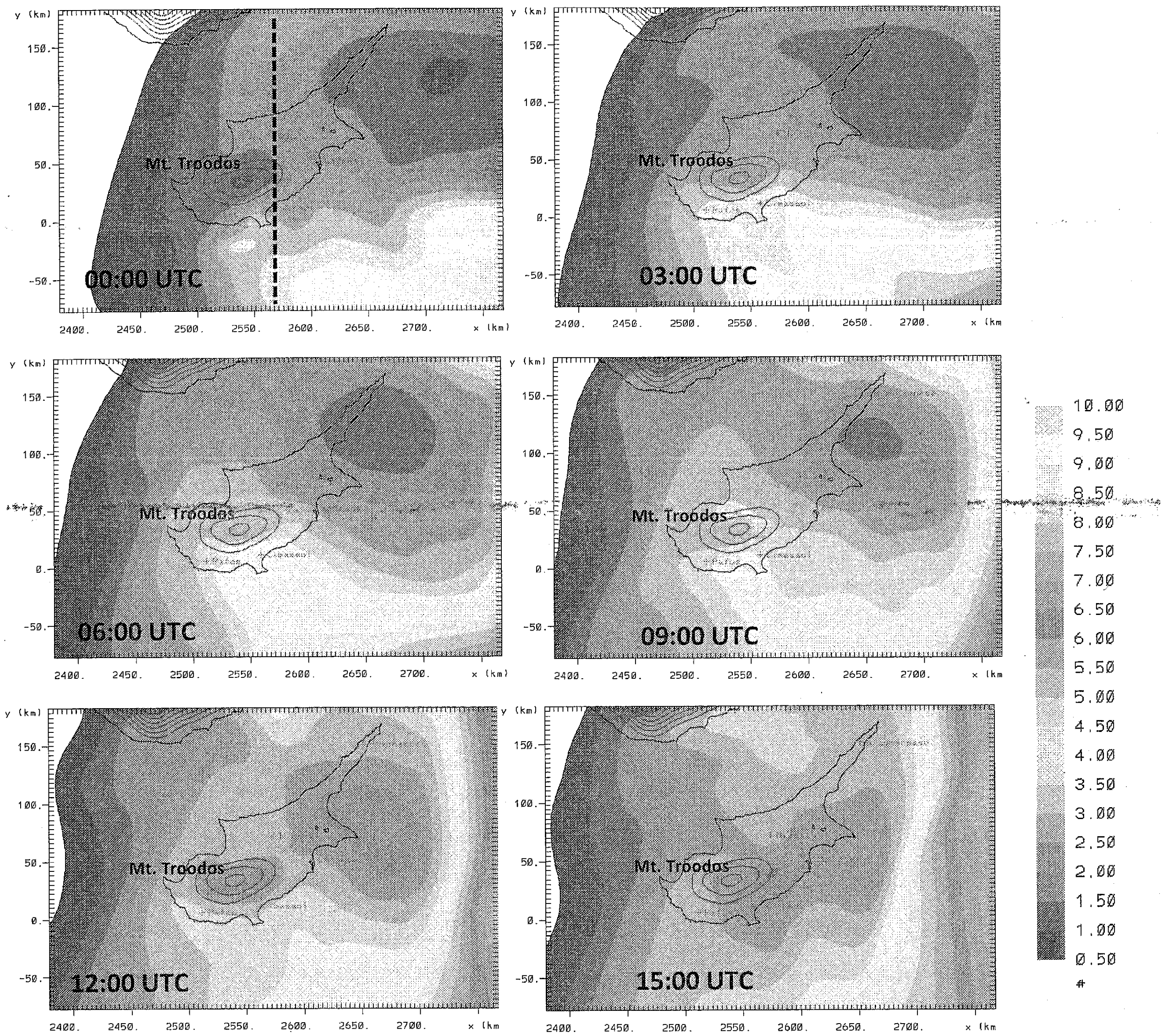

Figure12. Model 550 nm AOT over Cyprus 00:00 – 15:00 UTC, 8 September 2015, zoom from the second (4×4 km) model domain. The dashed black line shows the location of the cross-sections in Figure 13.

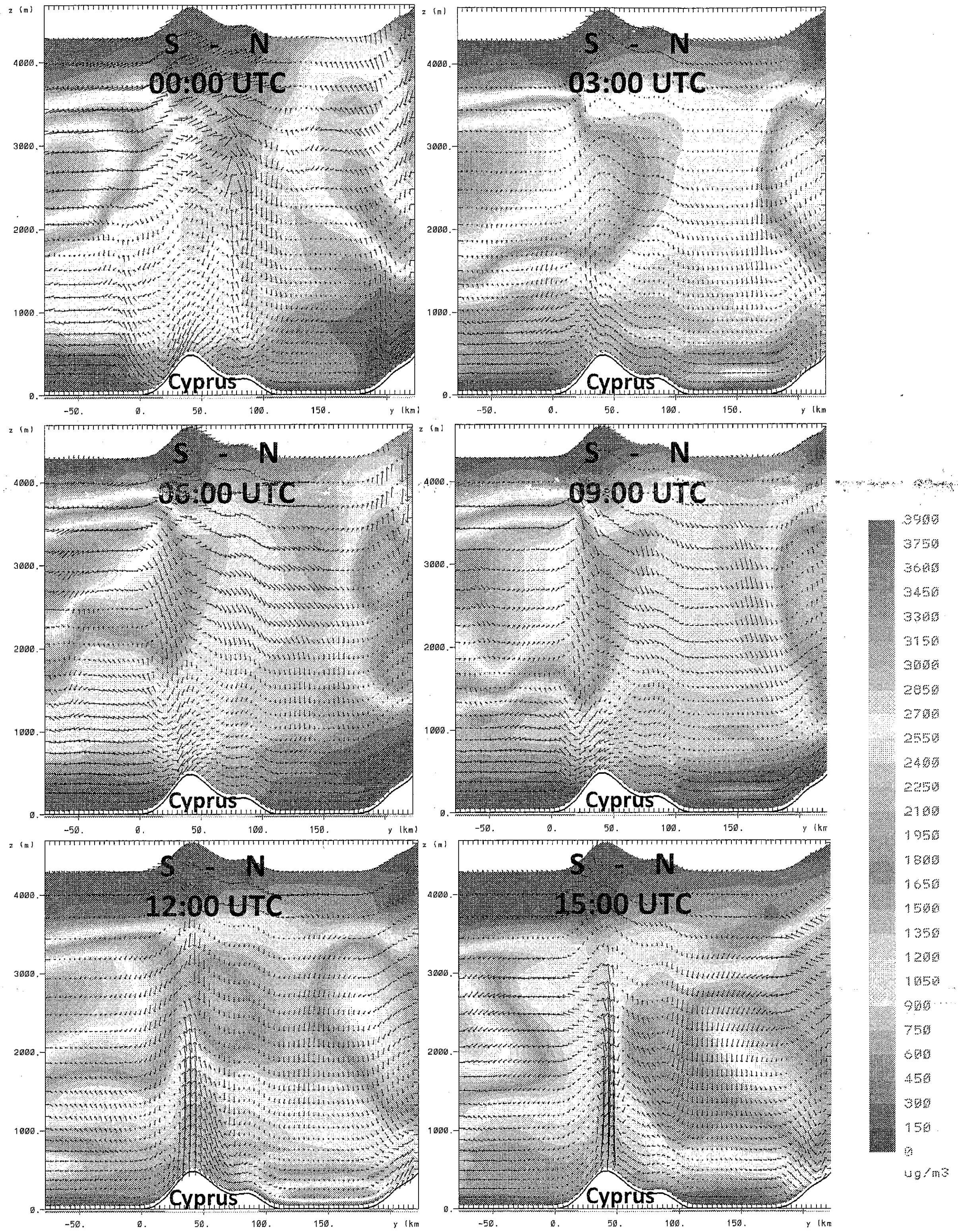

Figure 13. Vertical cross-section (South-North) of modeled dust concentration over Cyprus 00:00 – 15:00 UTC, 8 September 2015. The location of the cross-section is shown in Figure 12a.